Novel Printable and Tunable Bioresin with Strategically Decorated Molecular Structures

Celia Rufo-Martín[1,2,3], Diego Infante-García[4], José Díaz-Álvarez[3], Henar Miguélez[3], George Youssef[1,2,*]

[1]Experimental Mechanics Laboratory, Mechanical Engineering Department, San Diego State University, 5500 Campanile Drive, San Diego, CA, U.S.A.

[2]Advanced Manufacturing Hub, San Diego State University, 5500 Campanile Drive, San Diego, CA, U.S.A.

[3]Department of Mechanical Engineering, Universidad Carlos III de Madrid, Avda. de la Universidad 30, 28911 Leganés, Madrid, Spain

[4]Institute of Mechanical and Biomechanical Engineering, I2MB, Department of Mechanical Engineering and Materials, Universitat Politècnica de València. Camino de Vera, 46022 Valencia, Spain

Abstract

As personalized medicine rapidly evolves, there is a critical demand for advanced biocompatible materials surpassing current additive manufacturing capabilities. This study presents a novel printable bioresin engineered with tunable mechanical, thermal, and biocompatibility properties through strategic molecular modifications. We introduce a new bioresin comprising methyl methacrylate (MMA), ethylene glycol dimethacrylate (EGDMA), and a photoinitiator, which is further enhanced by incorporating high molecular weight polymethyl methacrylate (PMMA) to improve biostability and mechanical performance. The integration of printable PMMA presented several synthesis and processing challenges, necessitating substantial modifications to the 3D printing process. Additionally, the bioresin was functionalized with antibacterial silver oxide and bone-growth-promoting hydroxyapatite at various weight ratios to extend its application further. Our results demonstrate the agile printability of the novel bioresin and its potential for transformative impact in biomedical applications, offering a versatile material platform for additive manufacturing-enabled personalized medicine. This work highlights the adaptability of our novel printable bioresin for real-life applications and its capacity for multiscale structural tailoring, potentially achieving properties comparable to native tissues and extending beyond conventional additive manufacturing techniques.

1. Introduction

In the emergent field of personalized medicine, the development of advanced printable materials is paramount for novel therapeutic solutions, including radiotherapy wearables [1], drug delivery [2], anatomic models for agile surgery planning [3], and tissue-replacing implants [4]. Nonetheless, the state-of-the-art is eclipsed by the limited availability of viable material solutions, providing aseptic materials that are inconducive to advanced and personalized implants. For instance, available bioinert materials predominantly constrained cranioplasties [5], hindering transformative advancement in orthopedics using additive manufacturing. Therefore, we introduce a new class of advanced and printable resins, termed *osseoPRINT*, which transcends the state-of-the-art on multiple fronts, including (1) strategic integration of antibacterial and osteoinductive agents, (2) a streamlined synthesis process, (3) compatibility with 3D printing methodologies, and (4) versatility across various additive manufacturing techniques. The newly synthesized *osseoPRINT* resins surpass the bioinertness asymptote of the current barriers to personalized and translational medicine applications.

Research into advanced material systems aimed at accelerating personalized medicine has bifurcated into various directions, with some focusing on biology-based approaches (*e.g.*, extraction of biological tissues from animals matching humans [6] and stem cells [7,8]) and engineering-based directions (*e.g.*, bio-simulant materials with integrated cells [9], 3D printing of living organs [10], and advanced manufacturing of implants with complex geometries [11]). While biology-based approaches hold promise, their nascent stage and associated ethical concerns present significant hurdles to their practical application in clinical settings, *e.g.*, bedside treatments. In contrast, engineering advanced materials and structures for orthopedics offers a more immediately viable path due to their scientific, technological, and economic feasibility. At the forefront of advanced materials research, polymers (and their composites) are most suitable for the personalization of medical solutions, such as load-bearing implants, due to (1) processability [12], (2) mechanical and structural compatibility [13], (3) stability and tailorability [14], and (4) agility in rapid formulation and synthesis [14]. However, the development of bio-suitable and additively manufacturable polymers has been stagnant due to the limited availability of bioinert and bio-tailorable materials amendable to 3D printing.

Bioinert materials are the cornerstones in developing therapeutics from the onset of the personalized medicine paradigm, providing temporary and durable solutions to a diverse range of pathologies [15] [16]. In orthopedic ontology, mainly where regeneration is unviable or unavailable, polymers such as poly(methyl methacrylate) (PMMA), ultra-high molecular weight polyethylene (UHMWPE), and poly(ether-ether-ketone) (PEEK) are ubiquitous in load-

bearing orthopedics due to their biocompatible behaviors, commercial availability, bio-inertness, persistent stability, and reliable performance [17]. The side-effects of using these material candidates in orthopedics, including the conventional manufacturing and integration approaches, overshadow these advantages since it could potentially endanger the patients (*e.g.*, PMMA molding of implants might toxify insertion site with unterminated radicalized or uninitiated monomers, and the exothermic polymerization reaction) [18]. The advent of additive manufacturing (AM) is opportune for broader personalization for patient-specific orthopedics, strategic material decoration for multifunctionality, and, in turn, improving the quality of care and life [19] [20]. AM techniques trump the state-of-the-art in realizing complex structures with unprecedented geometrical tailorability derived directly from medical images [21]. Hence, AM, polymers, molecular decorations, and personalized orthopedics are the foundations for the presented advanced (and printable) material systems, *osseoPRINT*.

Among the various bioinert materials emulating the properties of bone, polymethylmethacrylate (PMMA) remains a prevalent choice for FDA-approved orthopedic and cranioplasty applications due to its thermomechanical stability, ease of photopolymerization, and minimal toxicity [22],[23],[24],[25],[26]. To further enhance its thermomechanical attributes, crosslinking PMMA with chemically and biologically compatible compounds has emerged as a strategic approach [27]. Ethylene glycol dimethacrylate (EGDMA), an oligomer, has been extensively studied in its polymerized state and demonstrated to be biocompatible and cell-friendly [28],[29]. Previous research has successfully employed EGDMA as a crosslinker for PMMA and methyl methacrylate (MMA) in implants to bolster their thermomechanical stability [30]. Moreover, incorporating nanoscale particles as molecular decorations into physically and chemically crosslinked PMMA and poly(MMA-*co*-EGDMA) can lead to a biomaterial with superior biocompatibility. Silver nanoparticles, known for their antibacterial, antifungal, and antioxidant properties, have been widely used as bio-fillers while exhibiting low cytotoxicity at appropriate concentrations [31],[32],[33]. Hydroxyapatite (HAp), a bio-ceramic that closely resembles the mineral composition of bone, promotes osteointegration by stimulating bone growth and osteoblast proliferation [34],[35]. HAp is a versatile material with numerous biomedical applications, such as surface modifications and functionalization for tissue engineering [36],[37]. While these compounds have been individually studied, this research, to our knowledge, presents the first report of a printable, biomaterial with tunable properties, incorporating the above-mentioned chemicals into a single formulation.

To placate the bio-inertness limitations in the current state-of-the-art, we have developed a novel class of advanced printable resins, *osseoPRINT*, with tunable thermomechanical and rheological properties enabled by solely adding antibacterial and osteoinductive agents (**Fig. 1**). The versatility of *osseoPRINT* is rooted in its additive-manufacturing-technique agnosticism by carefully optimizing the monomer-to-polymer ratios while avoiding rheological modifiers that compromise the resin biocompatibility and negatively alter the mechanical and structural responses. All rheological modifiers are eliminated from *osseoPRINT*, evidencing additional novelty of the research leading to this paper. The synthesis of *osseoPRINT* was easily optimized for vat photopolymerization (VPP) 3D printing, demonstrating the adaptability of the process without negatively reflecting on the mechanical performance. The fully integrated *osseoPRINT* resins were found suitable for producing intricate geometries of bone microstructure representations. Thus, our *osseoPRINT* resins are a facile and flexible solution for additive manufacturing advanced resin implants.

The processing-mandated viscosity of the base resin was achieved by tailoring the amounts of high-molecular polymethyl-methacrylate (PMMA) to a base of methyl-methacrylate (MMA) and ethylene glycol dimethacrylate (EGDMA), **Fig. 1a-*i***. The incorporation or absence of PMMA was reflected in a viscosity range between 0.04 and 14.60 Pa·s without affecting the synthesis or manufacturing process (**Fig 1a-*ii***). Printed plates exhibited an average storage modulus of 3.12 ± 0.13 GPa (**Fig. 1a-*iii***), further manifesting the manufacturing adaptability with stable mechanical properties independent of the PMMA concentration. Adding antibacterial and osteoinductive agents had a meager effect on the printable resin properties, irrespective of the nano-filler content (**Fig. 1b**). **Fig. 1b-*i*** compiles the different composition iterations and the slight change in viscosity through its lifetime, where 0 *wt.*% PMMA resin and 10 *wt.*% resin are the bounding compositions in terms of viscosity values (0.04 and 13.42 Pa·s before printing and 0.07 and 34.72 Pa·s after printing). The mechanical stability of the resin was maintained after hybridization, reporting a similar storage modulus of 3.15 GPa, on average, at body temperature (37 ºC), and only at high temperatures (un-physiological) was the behavior damped by the dopant agents (**Fig. 1b-*ii***). The thermal history of the composite (**Fig. 1b-*iii***) reported T_c = 116.4 ± 16.4 ºC and T_m = 264.2 ± 9.7 ºC, elucidating the possibility of using material extrusion as a manufacturing technique after the pelletization or spoolization of the *osseoPRINT*; an active area of research in our group. The successful printing of the miniaturized gyroid structures (**Fig. 1c**) ascertains the reality of implementing *osseoPRINT*, which reported compressive mechanical properties suitable for bone replacement applications. The selection of a gyroid triply periodic minimal

surface (TPMS) structure to emulate the bone is elaborated upon in the forthcoming sections, while compressive stiffnesses are compared to other engineered topologies. This advanced resin significantly enhances the translational potential for bone-replacement implants, offering exceptional adaptability and suitability across diverse manufacturing processes.

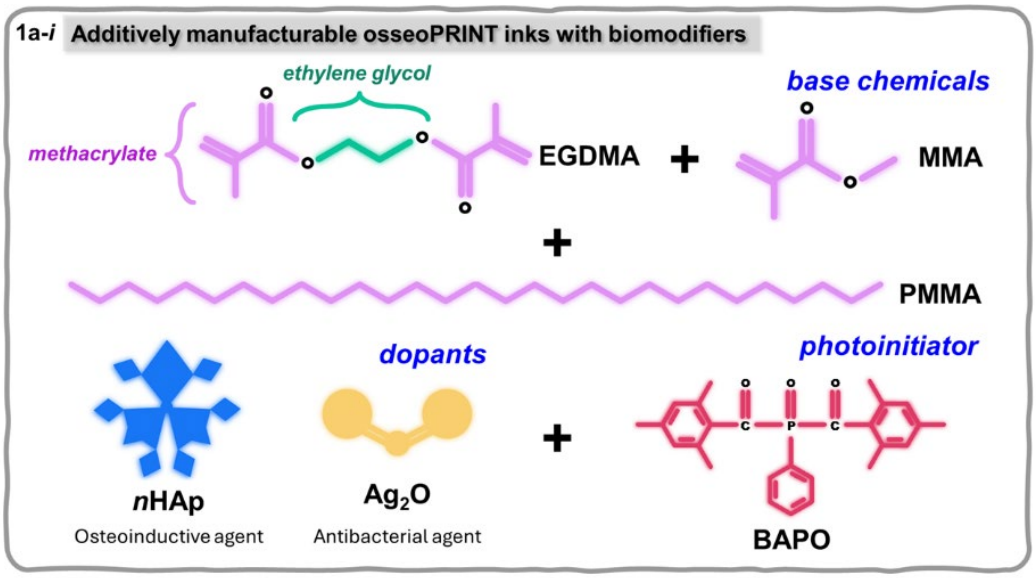

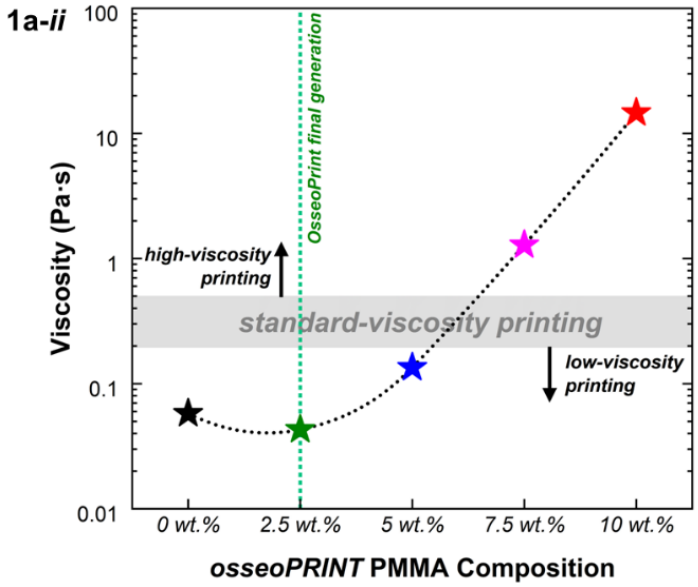

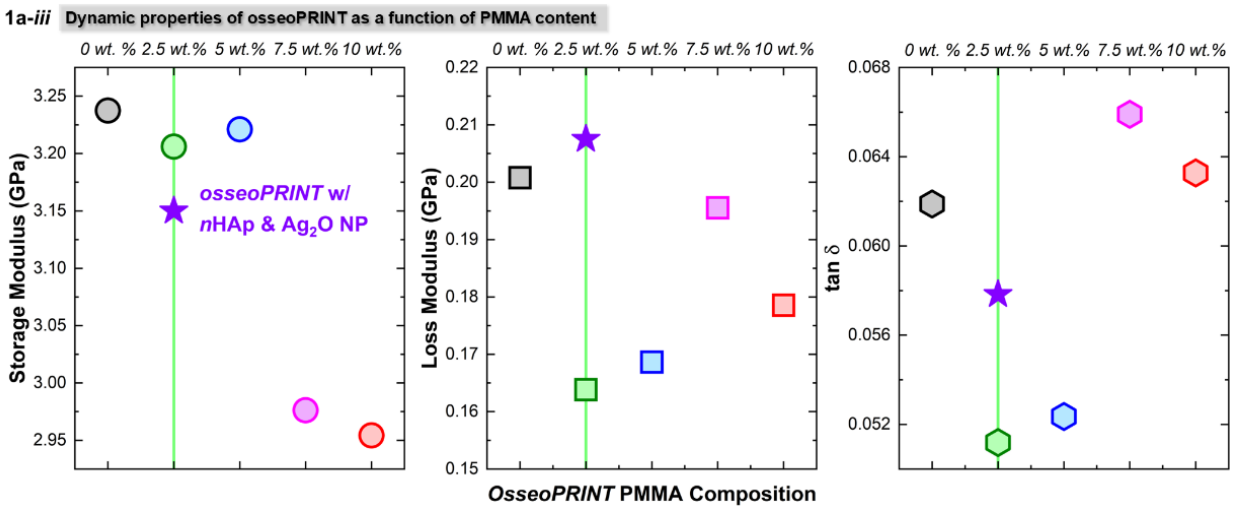
1a-iii
Dynamic properties of osseoPRINT as a function of PMMA content
0 wt. % 2.5 wt.% 5 wt.% 7.5 wt.% 10 wt.%
Storage Modulus (GPa)
osseoPRINT w/
nHAp & Ag2O NP
Loss Modulus (GPa)
tan δ
OsseoPRINT PMMA Composition

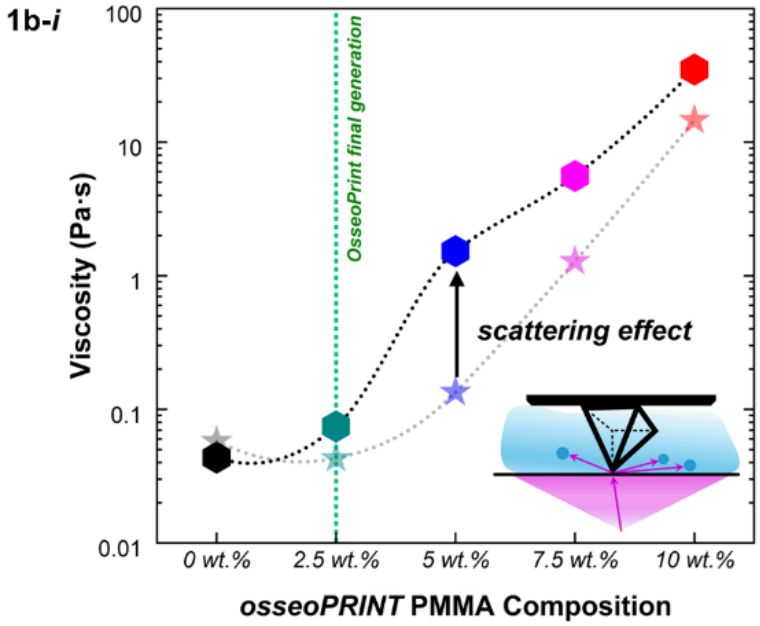
1b-i
Viscosity (Pa·s)
OsseoPrint final generation
scattering effect
0 wt.%
2.5 wt.%
5 wt.%
7.5 wt.%
10 wt.%
osseoPRINT PMMA Composition

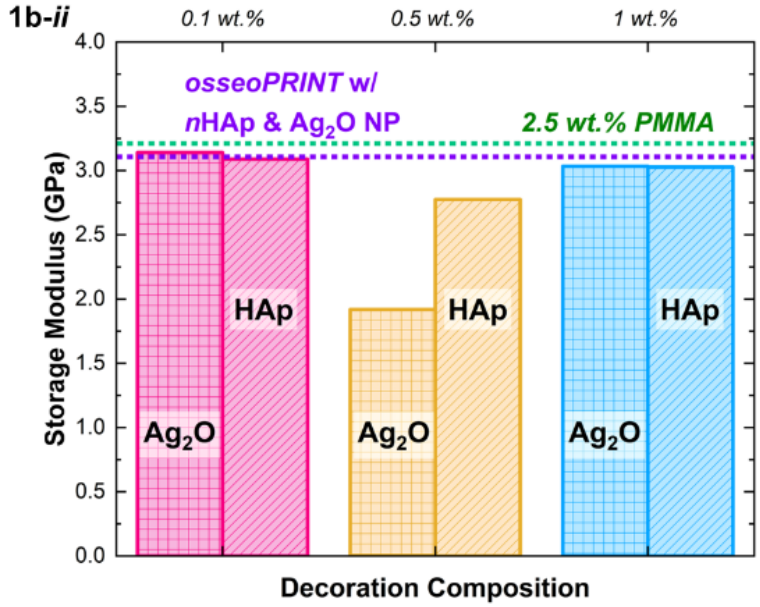
1b-ii
0.1 wt.%
0.5 wt.%
1 wt.%
osseoPRINT w/
nHAp & Ag2O NP
2.5 wt.% PMMA
Storage Modulus (GPa)
HAp
Ag2O
Decoration Composition

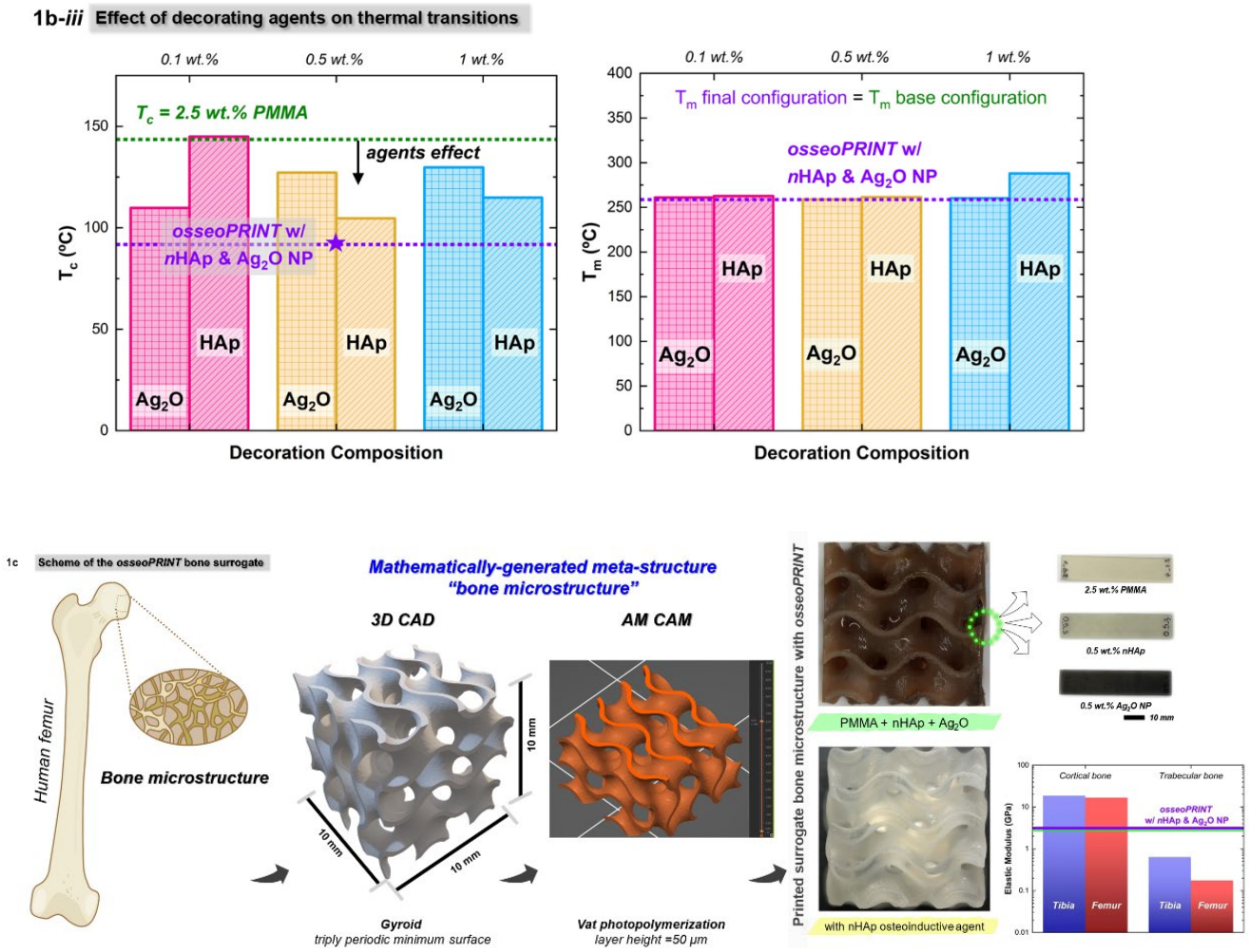

Figure 1. Novel printable and tunable bioresin (osseoPRINT) and its process-property interrelations. (a) Structure and molecular decoration of osseoPRINT resin generations, showing the integration of modifying nanoscale antibacterial and osteoinductive agents are additively manufactured using modified VPP 3D printing, rheological stability of printable bio-compatible osseoPRINT resins, and the dynamic properties of osseoPRINT samples at body temperature (37 ºC). (b) Process-property nexus of newly synthesized and printed bioresin, showing the influence of antibacterial and osteoinductive agents on (i) lifetime, (ii) mechanical properties, and (iii) thermal transitions (i.e., glass transition and melting temperatures). (c) Practical demonstration of streamlined bone replacement implants evidencing miniaturized gyroid structures (10 × 10 × 10 mm^3), epitomizing the agility and facility of novel osseoPRINT.

2. Results and discussion

2.1. Synthesis, printability, and lifetime of osseoPRINT

The synthesis of the first generation (neat versions) of *osseoPRINT* resins focused on creating a bioinert formulation suitable for personalized medicine applications while avoiding unnecessary chemical modifiers to mitigate potential toxicity and bio-rejection [38]. The neat version of *osseoPRINT* exhibits a broad and tunable range of rheological and mechanical properties by adjusting the weight ratio of PMMA powder, as delineated in §4. The base resin

was formulated by homogenizing MMA monomer and EGDMA in a 50:50 weight ratio followed by 180 s elliptical mixing with BAPO, resulting in the printable bioinert polymer (**Fig. 2a-*i***). To fine-tune the rheological properties and stabilize the chemical, thermal, and mechanical behavior of the base printable resin, PMMA powder (Ø = 100-250 μm) was added to the MMA/EGDMA solution at varying weight ratios, ranging from 0 to 10 *wt.*%, while continuously stirring in a heated water bath at 50 ºC for 210 min to balance between proper mixing and avoiding premature gelation due to the relatively low thermal stability of the PMMA [39]. The solubility of PMMA in the MMA monomer is highly dependent on the content ratio and the synthesis temperature to control the Trommsdorff effect. The latter prevents rapid polymerization, which, if occurred, leaves undissolved PMMA powder beads suspended (but hidden within the solution due to the refractive index matching) within the flash-cured gel [40]. The flash-cured gel exhibits ultrahigh viscosity, deeming it unmovable from the mixing container to the 3D printer, *i.e.*, compromising the feasibility of the 3D printing process. Hence, selecting the proper synthesis conditions (*e.g.*, temperature and stirring speed) is paramount for formulating 3D printable PMMA-based resins. The balanced conditions provide ample time to radicalize the PMMA chains within the MMA/EGDMA solution without inducing the complete polymerization reaction [40]. The final step is strategically adding the photoinitiator to the PMMA/MMA/EGDMA to induce radical polymerization upon ultraviolet exposure during 3D printing [41]. This carefully choreographed synthesis process resulted in the first generation of agile *osseoPRINT* resins (agility is defined as facile tunability), **Fig. 2a-*ii***, evidenced by the successful preparation of several batches.

The viscosity is the primary barrier to successful 3D printing of the *osseoPRINT* base resins using the VPP 3D printing process by dictating the critical processing parameters [42], such as approach and retraction speeds, layer height, and bottom layer exposure, to name a few [43]. To address this challenge, several modifications were made to standard VPP equipment: (1) printing was conducted under an inert nitrogen atmosphere by adding a purging mechanism to mitigate the reactivity of PMMA in ambient conditions [44], (2) printing parameters were optimized to accommodate the broad viscosity range associated with different PMMA concentrations, and (3) the incubation period between resin formulation and print initiation was carefully controlled. The printing process was performed in a nitrogen-filled environment to prevent organic volatiles from destabilizing the resin and impairing print quality. **Fig. 2a-*i*** shows a schematic of the printing procedure, where the resin was transferred to the vat, followed by purging the printing chamber with nitrogen at 0.75 MPa and 1.5 l/min for 10 min before starting the printing process. The same N_2 flow conditions were also maintained

throughout the additive manufacturing process to preserve the chemical stability of the resin and the printed artifacts. The heuristically optimized printing parameters include 30 s bottom exposure time, 10 s exposure time, and a platform speed of 4-6 mm/s. The printing lift (ν_l= 4 mm/s) and retraction (ν_r= 6 mm/s) speeds are correlated to a shear rate of $\dot{\gamma}$ = 1 and 1.5 s^{-1}, respectively, giving that $\dot{\gamma}=\nu_i/e$ (ν_i is the platform speed with the subscript $i = l$ for lift and r for retraction, and e is the layer height) [29]. The rheological properties and their relationship to the printing process as a function of PMMA concentrations are discussed next. The samples were then post-processed using the conditions delineated in the *Experimental Methods* section.

The rheological properties (**Fig. 2b-*i***) of the first-generation *osseoPRINT* resins (neat versions) provided additional insights into the dynamic mechanisms dominating the 3D printing process. On the one hand, the viscosity-shear rate interrelation is highly sensitive to the PMMA *wt.*%, where resins ≥ 5 *wt.*% PMMA exhibit quasi-Newtonian fluid behavior [45], while ≤ 2.5 *wt.*% PMMA demonstrates a pronounced shear thinning phenomenon [46]. This difference is attributed to the solute-solvent interactions stemming from the distinct molecular weight and chain mobility of the constituents, where increasing the *wt.*% of the high *Mw* PMMA hinders the free motion of MMA and EGDMA molecules [47]. The absence of significant PMMA content in *osseoPRINT* resins (*i.e.*, ≤ 2.5 *wt.*%) is conducive to solvent (MMA and EGDMA) breakdown that transpires as shear thinning [48]. The dichotomy between the resin viscosity as a function of PMMA, shear thinning to quasi-Newtonian transition, axiomatically manifested during the transfer from the mixing container to the printing vat, evidencing rapid FEP (fluorinated ethylene propylene) sheet wetting for resins with low *wt.*% PMMA to forced wetting (*i.e.*, forcibly spreading the resin onto the FEP sheet) for the higher *wt.*% counterparts. While the latter observation is anecdotal, it coincides with the rheological properties of the *osseoPRINT* resins. The printing shear rates correspond to a dynamic viscosity of 0.05 and 10 Pa·s, defying the limits of off-the-shelf resins for VPP (denoted on the corresponding figures of the rheological properties). In other words, our modified printing process readily accommodates the low viscosity resins (*i.e.*, *osseoPRINT* with ≤ 2.5 *wt.*% PMMA) and their higher viscosity counterparts (*i.e.*, *osseoPRINT* with ≥ 5 *wt.*% PMMA), remarkably without any alteration of the printing parameters. On the other hand, the shear stress (τ) is also related to the shear strain rate (and by induction to the printing speed) and viscosity, as shown in **Fig. 2b-*ii***. The importance of the shear stress ($\tau = \dot{\gamma} \times \eta(\dot{\gamma})$) epitomizes the spreading of the *osseoPRINT* resin during the additive manufacturing process as the printing platform regulates the layer height throughout the process (*i.e.*, retracting away from the FEP

sheet to allow the fresh resin to seep into the printing region and approaching the LCD screen to commence the exposure). Rheology is leveraged again to provide insights into this dynamic printing environment, where τ = 0.05 – 36 Pa within $\dot{\gamma} = 1$ and 1.5 s^{-1}, respectively, translating to shear strain ($\gamma = \int \tau/\eta(\dot{\gamma})\, dt$) in $\mathcal{O}(1)$ that indicates the spreading (**Fig. 2b-*iii***) of the resin within the printing area (60×12.9 mm^2). It is, however, imperative to reiterate that the additive manufacturing of *osseoPRINT* is classified as evolutionary since changes in the viscosity are temporal as a function of printing time and conditions, as discussed next.

The affinity of photopolymerizable *osseoPRINT* to ultraviolet radiation during the printing process affects the lifetime of the resin and, in turn, reduces the production yield from each batch. The interaction between the activating ultraviolet light rays (and their diffraction around the sample edges) results in the evolution of the dynamic viscosity as a function of time, deeming the resin unprintable after a few printing cycles. The diffraction of ultraviolet light within the resin container during printing inevitably results in the curing of the adjacent polymer voxels in the vicinity of edges and internal features, affecting the viscosity due to the immiscibility of polymerized particles. To ascertain the usable lifetime of *osseoPRINT*, the initial viscosity of each batch is compared to the remnant viscosity after three printing cycles, indicating the retention of idiosyncratic Newtonian or quasi-Newtonian properties (**Fig. 2b-*i***). The simple chemical decoration of the base *osseoPRINT* amplified the scattering effect during printing (inevitable curing during photopolymerization from scattered light), given the absence of light-obscuring particulates (pigments, modifiers, additives, *etc.*) [49], leading to increasing viscosity after each printing iteration, especially pronounced for resins with higher PMMA concentrations (**Fig. 2b-*ii***). This light-resin interaction phenomenon (schematics shown in the inset in **Fig. 2b-*iii***) was axiomatic in resins with ≥ 5 *wt.*% PMMA, which, despite initially fulfilling the viscosity requirements for successful VPP manufacturing, becomes futile upon repeated usage. Otherwise, the tempered influence of ultraviolet on PMMA-based resins affirmed their suitability for further decoration with osteoinductive and antibacterial agents, as discussed next. Consequently, 2.5 *wt.*% PMMA *osseoPRINT* resin emerges from all other PMMA concentrations as the most viable option for printing structures with tunable and customizable biomedical attributes. It is worth noting that investigating *osseoPRINT* with different PMMA concentrations led to identifying the suitable content ratio for the following printable resin generation, *i.e.*, an informal optimization approach.

The second generation of *osseoPRINT* resin focused on improving the potential acceptability of this novel material by the human body, such that adding antibacterial and

osteoinductive agents to the substratum (*i.e.*, the base resin) enhanced the biomechanisms for proper integration. The selection of the specific decorating compounds was discussed in the introduction, motivated by previous research that investigated them separately for biomedical applications. The formulation of this version of *osseoPRINT* (*i.e.*, individually including antibacterial and osteoinductive agents) faithfully followed the steps used to prepare the base resins with two minor modifications. Here, progressive tailoring of the formulation was imperative to accentuate the stability of the final printable resin. The first modification entailed the addition of mineralized hydroxyapatite nanoparticles (*n*HAp) at weight ratios of 0.1, 0.5, and 1% with respect to the total weight of MMA/EGDMA/PMMA(2.5 *wt.*%). The upper bound of *n*HAp hybridization balances between sufficient potential osteointegration [50], matching mechanical properties of the native tissue [51], and subduing light diffraction from the particles during printing (*i.e.*, achieving printability and biointegration synchronously). The *n*HAp dopant was added to the printable base resin with 2.5 *wt.*% PMMA in the planetary mixer for 240 s, followed by a 24-hour resting period based on a twofold rationale. This resting period was crucial to properly distributing and stabilizing the *n*HAp within the resin matrix.

The initial mixing of the *n*HAp with the base resin in the planetary mixer is predominately dictated by the Marangoni flow [52], resulting in an apparent homogenized solution with the osteoinductive agent fully suspended throughout. However, HAp nanoparticle agglomerates tend to rapidly settle at the bottom of the mixing vial due to Stokes settling ($u = g \cdot d^2 \cdot (\rho_s - \rho_l)/(18\mu)$, where g is gravitational acceleration, d is the particle diameter, ρ_s and ρ_l the particle and the liquid densities, respectively, and μ the viscosity) [53]. The settling velocity is directly proportional to the squared diameter ($\mathcal{O}(10^{-9}\ m)$) and inversely related to the dynamic viscosity ($\mathcal{O}(10\ mPa.s)$), resulting in settling time $\mathcal{O}(3000\ s)$ that coincides with the visual estimation of the settling during the synthesis process. Notably, after 24 h, the *n*HAp percolated throughout the solution, resulting in a two-phase system in which the smaller diameter particles were suspended in an equilibrium between weight-penalized drag ($F_d = 1/2\ C_d V^2 \rho A + mg$, where C_d is the drag coefficient, V the velocity, ρ the density, A the area, m the mass, and g the gravity) and floating-induced buoyancy ($F_b = -\rho g V$) forces [54] [55]. The larger *n*HAp particles remained settled (**Fig. 2c-*i***). **Fig. S2** and **Fig. S3** in the *Supplementary Document* depict a model describing the settling and percolation processes, leading to a printable hybridized resin (*n*HAp + MMA/EGDMA/PMMA(2.5 *wt.*%)).

The second modification incorporated the antibacterial agent, Ag_2O, in the same ratios as *n*HAp nanoparticles in MMA/EGDMA/PMMA(2.5 *wt.*%) base resin. Ag_2O nanoparticles,

in controlled concentrations, exhibit remarkable antibacterial properties with proven lower infection rates in integrated orthopedics, as discussed in the introductory remarks [56], but high concentrations adversely toxify osteoblasts [57]. Hence, the upper bound of Ag_2O nanoparticle concentration was limited to 1 *wt.*% and the lower bound to 0.1 *wt.*% since reduced silver content is deemed futile. The additive manufacturing process also constrained the controlled concentrations of Ag_2O nanoparticles due to the light-nanoparticle interactions (*e.g.*, diffraction and scattering) [58]. The Ag_2O- MMA/EGDMA/PMMA(2.5 *wt.*%) hybrid resin was also left to rest *ca.* 24 h before printing based on the physical phenomena discussed above. The *n*HAp powder resulted in a slightly higher viscosity (**Fig. 2c-*ii***) than Ag_2O nanoparticles due to the differences in atomic weight. The printing parameters were slightly modified to accommodate the new decorations based on liquid-solid and light-resin interactions, leading to 80 s bottom exposure time and 30 s exposure time. All other parameters remained unchanged. The lifetime expectancy (comparing left and right panels in **Fig. 2c-*ii***) of the second-generation *osseoPRINT* resins was consistent with previous estimations. A final resin configuration was synthesized and additively manufactured, leveraging the optimized properties of earlier generations. The final *osseoPRINT* version comprises 0.5 *wt.*% *n*HAp and 0.5 *wt.*% Ag_2O nanoparticles in MMA/EGDMA/PMMA(2.5 *wt.*%) to balance printability, desired properties, and lifetime.

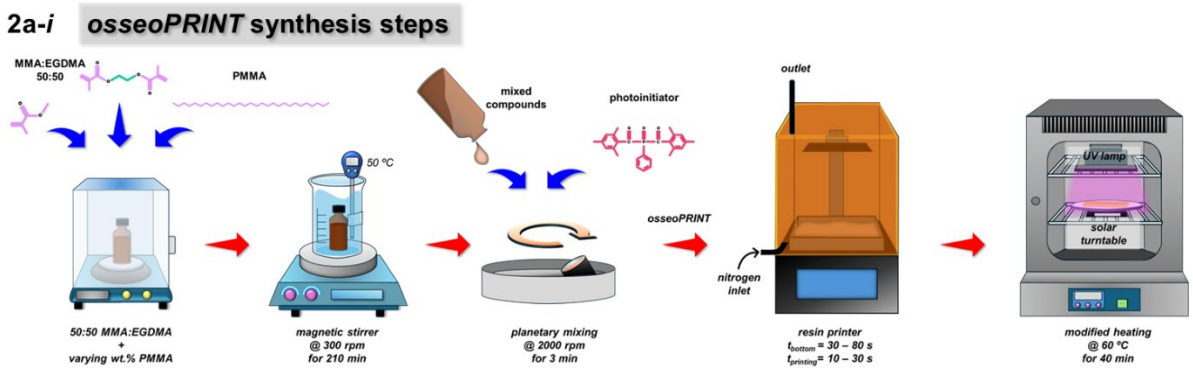

2a-*ii* ***osseoPRINT* chemical structure**

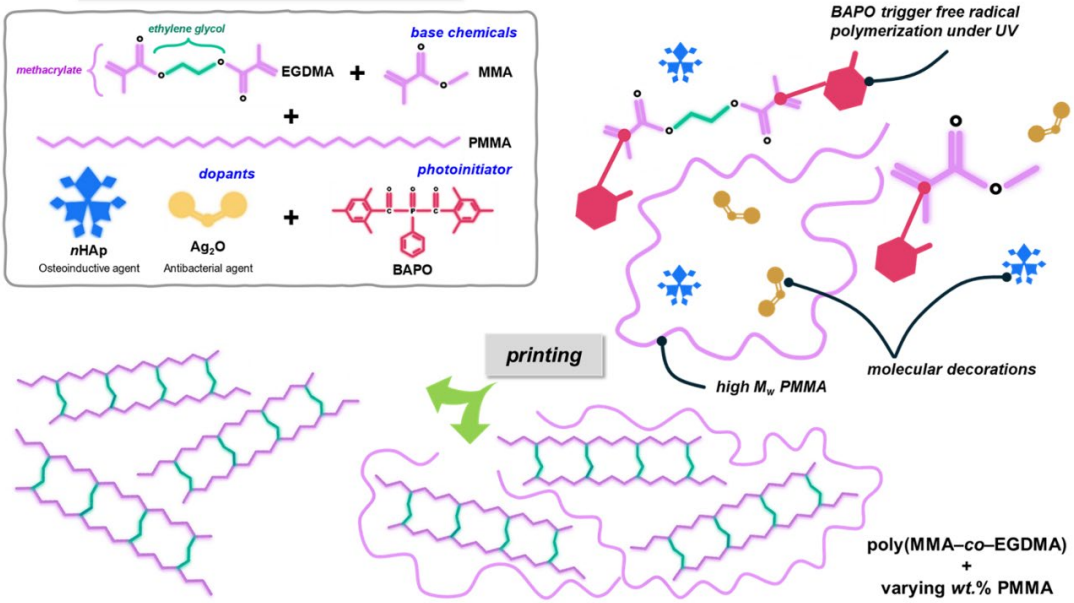

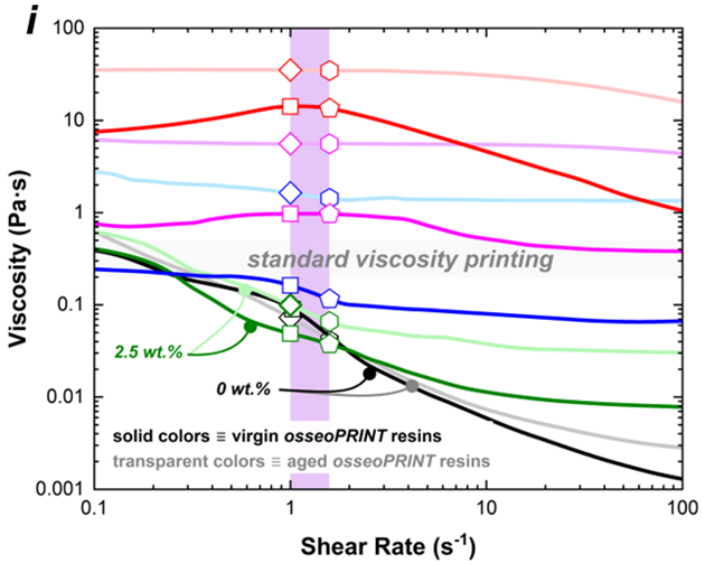

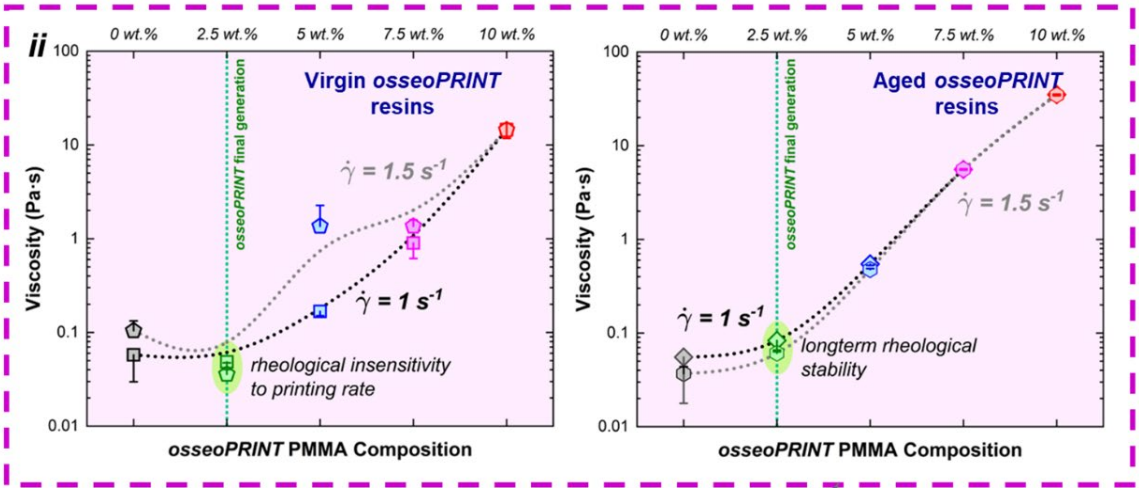

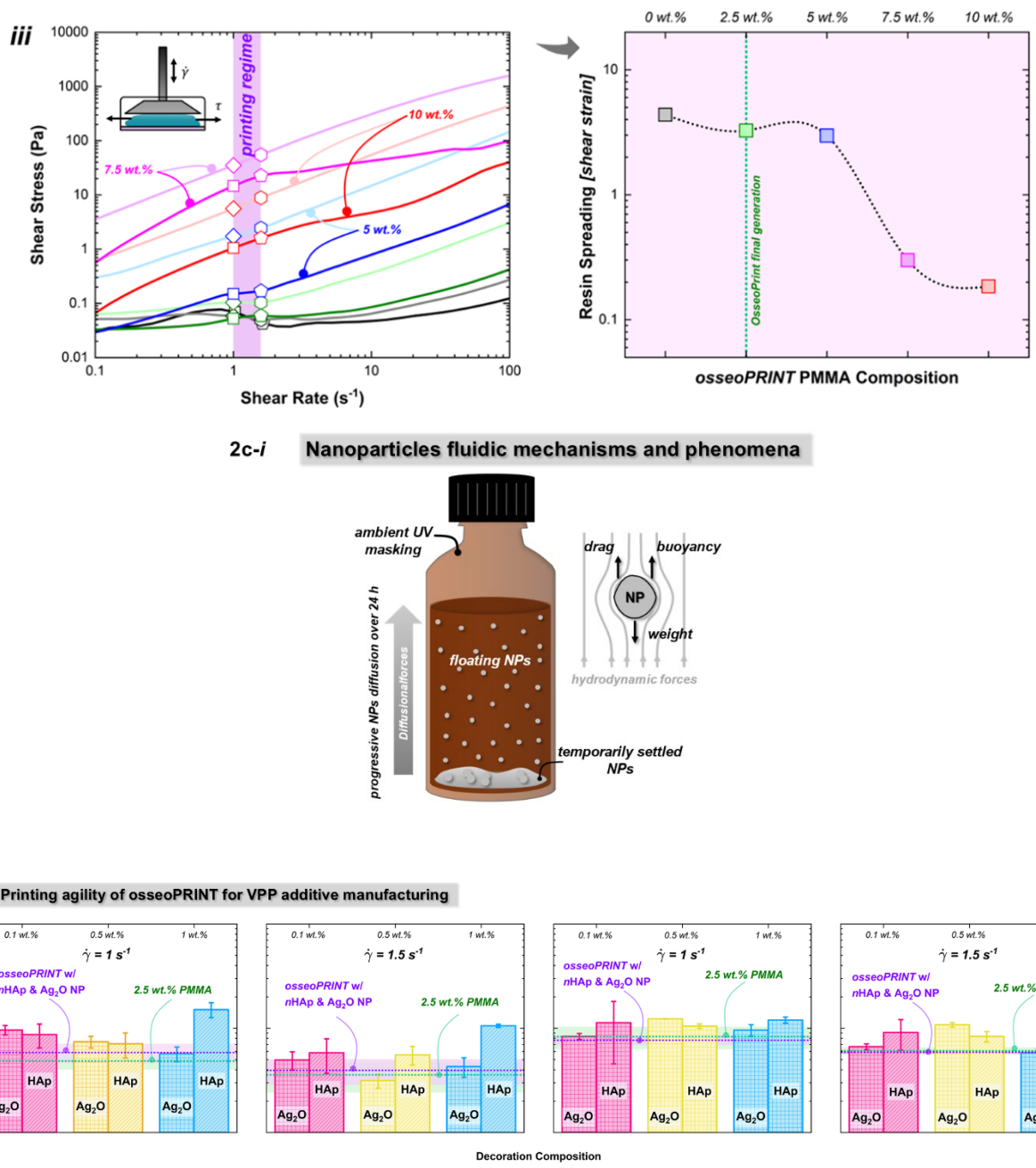

Fig. 2. The synthesis, physics, and rheology of tunable and printable decorated photocurable bio-suitable (osseoPRINT) resins. (a) Bench formational of osseoPRINT resulting in agile preparation and printing protocols. (b) Rheological underpinnings of poly(MMA-co-EGDMA)+PMMA photopolymrs, including viscosity and shear stress, are required to define printing parameters, lifetime, and spreading for handling during transport and processing. (c) Transport phenomena associated with the addition of nanoparticle decorations and the resulting rheology of the enhanced osseoPRINT with nHAp and Ag_2O modifying bioagents.

2.2. Multi-physical property mapping of osseoPRINT resins

The chemical integrity and signature of the 3D printed *osseoPRINT* resins were ascertained using FTIR-ATR, as discussed in the *Experimental Methods* section. The spectral peaks in **Fig. 3a** are primarily characteristic of PMMA and EGDMA [59], with an emphasis on the C-H stretching vibrations from the carbonyl group, primary polymer chain, and pendant methyl groups (λ=2945 cm^{-1}) [60], the C=O group (λ=1719 cm^{-1}) [59,60], [61], [62], the C=CH_2 stretching (λ=1636 cm^{-1}) [59], the C-CH_2 and C-CH_3 bending (λ=1445 cm^{-1}) [61], the C-O-C asymmetric stretching (λ=1145 cm^{-1}) [61], the O-CH_3 rocking (λ=960, 980 cm^{-1}) [59], and the C-C skeletal mode (λ=748 cm^{-1}) [61], [63], [60]. The decorated printed samples inherited the spectra of the 2.5 *wt.*% PMMA base resin, replicating the spectral peaks shown in **Fig. 3a-*i***. The hydroxyapatite concentrations (specifically 1 *wt.*%) exhibited a noticeable peak centered at 574 cm^{-1}, attributed to the bending of the PO_4^{3-} group [64] [65]. The spectroscopic results confirm the anticipated chemical structure, including that of the osteoinductive and antibacterial agents.

DSC study elucidated the molecular interactions between poly(MMA-*co*-EGDMA) and PMMA. The DSC thermograms are based on the first heating cycle at a rate of 3 ºC/min and show the suppression of T_g, which is influenced by the chain tacticity and heating rate [66] [67] [68] [69] [70] (**Fig. 3b-*i***). The crystallization temperature varied between 93.2 ºC and 143.6 ºC, with 10 *wt.*% PMMA resin showing the lowest value (**Fig. 3b-*ii***) due to the amorphous structure at increased content ratios. At the end of the thermal history, two peaks were observed: the first peak corresponds to the melting temperature (T_m), and the second was attributed to the thermal decomposition. T_m exhibited minimal variation across all *osseoPRINT* configurations (averaging around 260 ºC as depicted in **Fig. 3b-*iii***), yielding higher values than pure PMMA due to the apparition of crosslinking sites [71]. In the molecularly decorated configurations, the Ag_2O melting point emerges after the base polymer T_m but is only discernible in those resins with high compound concentrations. The diminution in T_m accentuates changes in PMMA molecular weight during the 3D printing process, which restricts molecular mobility and free volume due to the polymerization of poly(MMA-*co*-EGDMA), leading to a decrease in enthalpy during the non-isothermal process [72] [73]. The second endothermic peaks, centered around ~320 ºC, are attributed to the thermal decomposition due to carbonization, evidenced by notable color changes on the polymer powder beads remaining in the pan after testing (**Fig. S7** in the *Supplementary Document*). The endothermic decomposition peaks apodictically ascertain the thermal stability of the 3D-printed polymers and corroborate the accompanying DMA analysis.

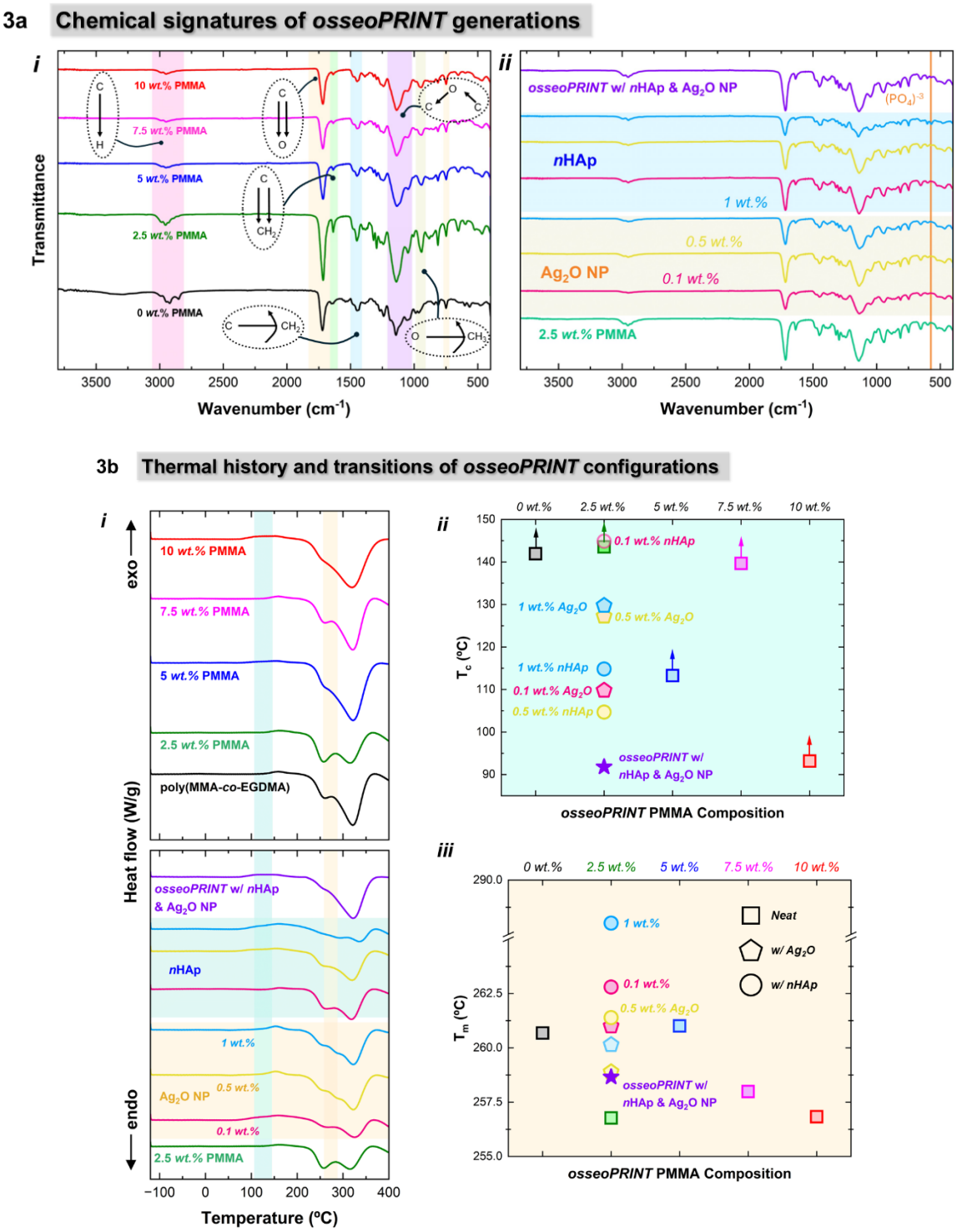

Fig. 3. Physicochemical and thermal properties of neat and decorated osseoPRINT resins. (a) Chemical signatures (FTIR-ATR spectra) of all osseoPRINT configurations show the chemical stability of the printable base resins (a-i) and the molecular decorated (a-ii). (b) Thermal history of the powderized osseoPRINT printed resins(b-i), including the effects of nHAp and Ag_2O nanoparticles on the crystallization (b-ii) and melting temperatures (b-iii), overall indicating biothermal stability in implant conditions.

The primary foreseen application for the photocurable *osseoPRINT* resins is skeletal implants adjacent to the native bone tissue, stipulating the need to match their mechanical properties

closely: (i) congruent mechanics to avoid stress shielding [74], (ii) nanoscale tailorability and decorations to improve acceptability and lifetime [75], and (iii) comparable time-dependent attributes (viscoelastic behavior) to gracefully manage dynamic loading scenarios (*e.g.*, mundane, leisure, or occupational movements) [76]. The mechanical response of all *osseoPRINT* generations was thoroughly investigated using dynamic mechanical analysis (DMA) and nanoindentation, as discussed in the *Experimental Methods* section. In DMA testing, the samples were loaded in the double cantilever configuration with 10 μm amplitude at 1 Hz and temperature ramp from 26 ºC to 190 ºC, reporting the storage modulus (E'), loss modulus (E''), and $tan(\delta)$ in **Fig. 4a-*i***. Irrespective of the *osseoPRINT* resin generation, the storage and loss moduli exhibit a decaying behavior as a function of temperature leading away from the glassy region, accentuating the previous discussion based on the physicochemical signatures. The decaying trend in the moduli reveals the complex structure of the resulting macromolecule, inheriting the attributes of linear and crosslinked polymers that stem from photopolymerization during printing. The printed and cured osseoPRINT structure is a byproduct of the chemically crosslinked poly(MMA-*co*-EGDMA) and physically crosslinked high-molecular PMMA chains, as elaborated upon in the *Supplementary Document*. Undecorated *osseoPRINT* resins ≤ 5 *wt.*% PMMA demonstrated higher amounts of crosslinking sites, resulting in a 50% drop in E' during the glass-to-rubber transition (*i.e.*, E' = 3.22 GPa in the glassy regime → E' =1.63 GPa in the rubbery plateau). The 7.5 *wt.*% and 10 *wt.*% PMMA reduced the storage modulus by 82% and 76%, respectively (0.44 and 0.72 GPa). The dependence on the PMMA content ratio is explicated based on reducing the number of crosslinked chains and, consequently, allowing more molecular mobility within the chemically and physically crosslinked macromolecule [77]. All first-generation prints using neat *osseoPRINT* versions demonstrated good mechanical and geometrical stability at relatively higher temperatures, amending the typical properties of neat, amorphous PMMA [78]. This thermomechanical endurance also transpired in E'', and apodictically in $tan(\delta)$, with limited activation energy dissipation mechanisms, evidencing predominantly elastic behavior and negligible dampening [79]. The effective modulus ($E_{eff} = \sqrt{E'^2 + E''^2}$) is insensitive to E'' such that $E_{eff} \approx E'$ throughout the thermal history except for the transition regime. Nonetheless, E'' and $tan(\delta)$ as a function of temperature further confirm the physical and chemical crosslinking duality of *osseoPRINT* resins. In the case of 0 *wt.*% PMMA, the manifestation of a single peak centered at 97.4 ºC corresponds to the glass transition temperature of the poly(MMA-*co*-EGDMA), while two

transitions coexisted for resins ≥ 2.5 *wt.*% PMMA at 68.2 ºC (for poly(MMA-*co*-EGDMA)) and 129.1 ºC (for high-*Mw* PMMA), pointing to a pseudo block copolymer structure.

The thermomechanical behavior of *osseoPRINT* resins (**Fig. 4a-*ii***) remained unchanged after adding the antibacterial agent (Ag_2O) due to the monodispersity of the nanoscale particles and the crosslinking duality of the underlying pseudo copolymer. This is remarkable since hybridizing the base resins for advanced biofunctionality proved effective in maintaining thermal (including transitions), chemical (spectral peaks), and mechanical (viscoelastic) stabilities. The Ag_2O nanoparticles act as non-impeding pinning sites, allowing the chain mobility afforded by the molecular structure, as discussed above, while inducing an antibacterial shield over the printed artifacts [80]. The addition of the *n*HAp osteoinductive agent, on the other hand, significantly reduced E' throughout the entire thermal history (**Fig. 4a-*iii***), effectively acting as stress-transfer inhibitors (*i.e.*, nanoscale inclusions) [81]. This interaction is rationalized based on twofold reasoning: (1) nonconformable and (2) ununiform geometry of the *n*HAp particles. The former (nonconformal) is substantiated by the distinct mechanical properties of *n*HAp (E = 114 GPa and ρ = 3.14 g/cm^3) compared to the surrounding polymer matrix and their chemical incompatibility. The *n*HAp particles remain suspended but unreactive to the polymer, evidenced by the unchanged physicochemical signatures. The *n*HAp particles, at the lower size limit, may also pin the relative molecular motion and positively affect the resistance to deformation in low loading regimes. The ununiform morphology implies possible poor adhesion between the *n*HAp particles and the resin [82], leading to partial or complete debonding such that the osteoinductive fillers resemble voids that compromise the stiffness, E' [83]. However, dampening is oblivious to the net effect of hybridization with *n*HAp given the heterogeneous interactions and polydispersity of the filler. These several *osseoPRINT* generations are suitable for biomedical implants (*e.g.*, dental, cranioplasties, and maxillofacial). Still, the final variation with *n*HAp osteoinductive and Ag_2O antibacterial agents exemplifies the ultimate solution for implants with complex biointegration functionality. The resulting effective modulus at body temperature, $E_{eff} \approx 3GPa$, is remarkably similar to the native bone stiffness (even without structural enhancements, as discussed next). *osseoPRINT* resin with *n*HAp and Ag_2O transcends the state-of-the-art in mechanics and performance while accounting for advanced manufacturability and printability, meeting the high aspirations of practitioners (surgeons and biomechanicians alike).

Finally, complete and successful biointegration stems from the nanoscale mechanical properties that promote ingrowth and bio-acceptance. **Fig. 4b** summarizes the nano-mechanical

properties of *osseoPRINT* resins leading to the final generation (*i.e.*, 2.5 *wt.*% PMMA base resin, 0.5 *wt.*% *n*HAp, and 0.5 *wt.*% Ag_2O separately and hybridized into fully integrated *osseoPRINT* resin). The nano-hardness of *osseoPRINT* resins are 0.25±0.04 GPa, **Fig. 4b-*i***, compares well with those of human bones (*ca.* 0.4-0.6 GPa), eclipsing the mechanical incompatibility in the bone-implant interfaces in current metal-bone or ceramic-bone solutions [84] [85]. The hardness of *osseoPRINT* is a byproduct of the base polymer (0.22±0.14 GPa), Ag_2O antibacterial nanoparticles due to its crystalline structure (0.24±0.03 GPa), and the *n*HAp osseoinductive agent with nearly similar structure as the mineralized calcium found in bone tissues even at low content (0.32±0.04 GPa). The corroboration of the hardness values between the native bone and the newly introduced *osseoPRINT* diminishes the potential of fretting wear in articulating joints or contact regions, leading to better biointegration by forming quick and firm interlocking connections [86]. Hence, meso- and micro-scale mechanics are also imperative for biomechanical compatibility [87], *i.e.*, mechanochemical interlocking.

The nanoscale reduced modulus ($\frac{1}{E_r} = \frac{1-\upsilon_{resin}^2}{E_{resin}}$, since the properties of *osseoPRINT* << than those of the indenter and assuming $\upsilon = 0.4$) was 5.16±0.46 GPa, closely resembling bone tissue at sites such as the cranium [88]. The molecular structure decorations using *n*HAp and Ag_2O nanoparticles corresponded to a unique alteration of the nano-mechanics, where the former enhanced the stiffness of the base resin (E = 4.95±0.20 GPa without *n*HAp → 5.73±0.49 GPa with 0.5 *wt.*% *n*HAp). Adding Ag_2O nanoparticles softened the nanoscale behavior (E = 4.95±0.20 GPa without Ag_2O → 4.68±0.28 GPa with 0.5 *wt.*% Ag_2O). Such alteration also manifested in the indentation work, culminated in the elastic and plastic works (**Fig. 4b-*ii***), where adding *n*HAp filler subdued the plastic work to merely 89.51±7.53 nJ compared to 112.96±1.73 nJ and 116±3.97 nJ for the undecorated and Ag_2O-only decorated resins, respectively. The effect of 0.5 *wt.*% Ag_2O nanoparticles and 0.5 *wt.*% *n*HAp in the final resin configuration resulted in 120.10±8.77 nJ of plastic work (primarily due to the former) and 68.16±1.32 nJ of elastic work (culminating the contribution of all the decoration agents). In all, the nanoscale mechanics corroborate the conclusions based on all previous characterizations, substantiating the biomechanical superiority of the 3D printed *osseoPRINT* resins as an advanced material system, accelerating the translational potential of the next generation of biomedical implants while emphasizing personalized medicine.

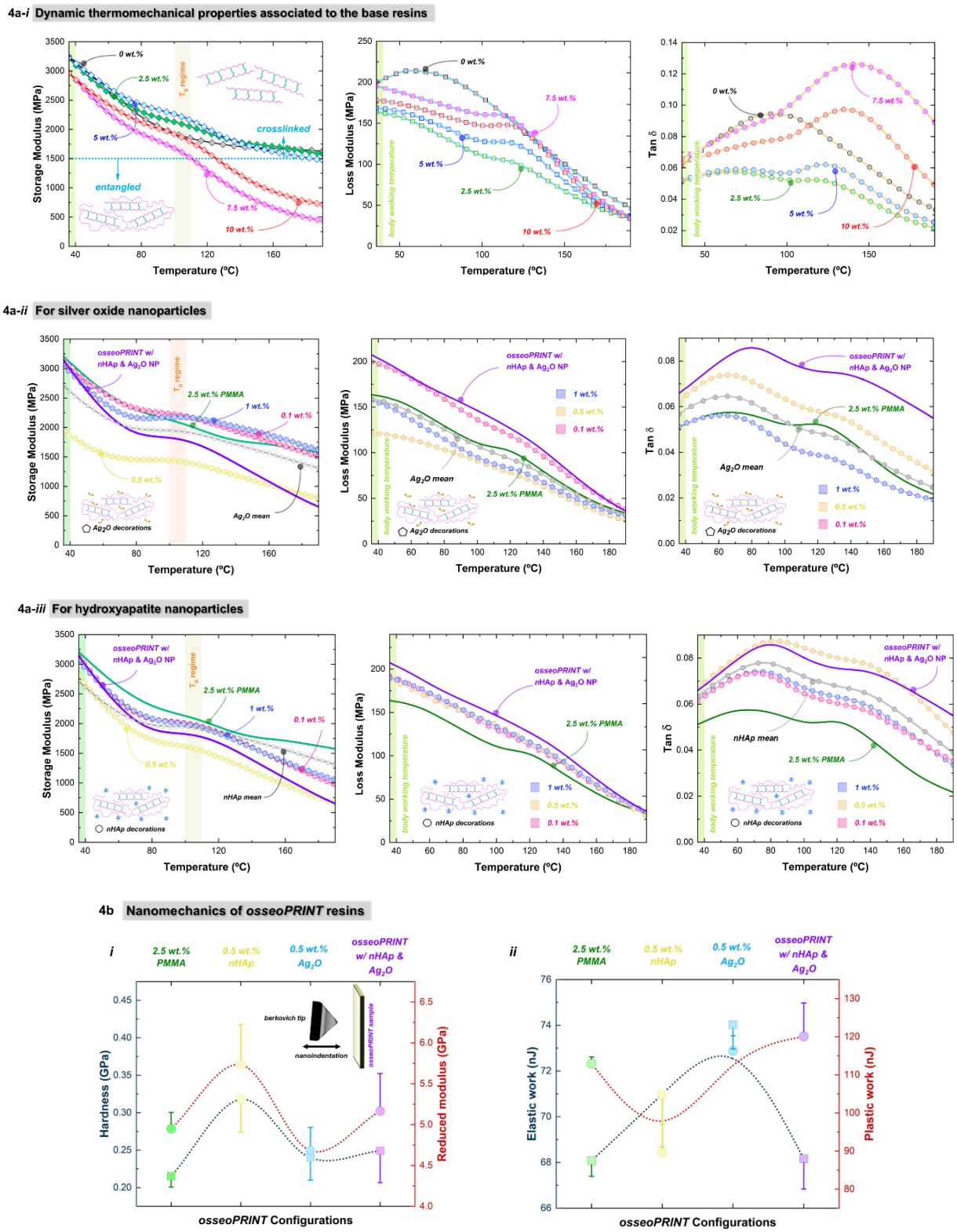

Fig. 4. Thermomechanical properties of neat and decorated osseoPRINT resins for bioimplants in personalized medicine. (a) Dynamic thermomechanical behavior of the printed osseoPRINT plates as a function of temperature, including the performance metrics of stiffness and dampening with emphasis on mechanical performance at body temperature: a-i the response from base resin as a function of PMMA wt.%, a-ii Ag_2O nanoparticles, and a-iii nHAp. (b) Nanomechanics of osseoPRINT samples, elucidating the interrelation between nanoscale hardness, modulus, b-i, and elastic/plastic energy, b-ii, with essential nanoparticle decorations (nHAp and Ag_2O).

2.3. Personalized medicine translational potential of osseoPRINT resins

To confirm the applicability of our *osseoPRINT* resins for personalized medicine implants with tailorable topologies, we successfully 3D printed bone surrogate meta-structures to explore the mechanical performance. The intricate geometry of bone tissue and its relationship with the topology of the implant [89] are paramount to proper osseointegration and avoiding detrimental phenomena such as the prolonged presence of a fibrous capsule-induced pain or loosening [90]. Mathematically generated meta-structures, *e.g.*, triply periodic minimal surface (TPMS) structures, have emerged as viable bone surrogate topologies for skeletal implants based on the congruency between the computer-generated geometries and natural bone microstructures. TPMS meta-structures are innovative topologies due to their interconnected porous diploë-like architecture [91], eclipsing state-of-the-art limitations such as reducing stress concentration, zero average curvature, and open porous structure [92],[93]. The unique attributes of the explored TPMS scaffold porosity assist cell migration and vascularization for better osseointegration while mitigating stress-shielding [94]. Notably, the selected TPMS scaffold is a demonstrative testbed for this printable advanced material, while other TPMS geometries can be readily fabricated and characterized. To exemplify and demonstrate the applicability of the *osseoPRINT* resins, a 10 × 10 × 10 mm^3 gyroid structure (**Fig. 1c**) was 3D printed using the modified VPP process and decorated bioresin with 0.5 *wt.%* *n*HAp and 0.5 *wt.%* Ag_2O. The compressive force-displacement response of the 3D printed fully decorated miniaturized gyroid is shown in **Fig. 5a**, resulting in a compressive stiffness of 734 ± 7.5 N/m based on the delineated linear response after the initial toe region. The miniaturized gyroids failed at a compressive force of ~370 N after nearly 1 mm compressive deflection, which can be further optimized via formal algorithms as part of future incremental developments. To facilitate the latter, the compression response was numerically simulated using finite element methods (Abaqus®) by ascribing comparable boundary conditions to those imposed during the experiment and assigning the properties deduced from the comprehensive testing regiment discussed above. Notably, the exact solid model used in VPP printing of the gyroid structure was used in the computational simulation. The effective modulus was adjusted for inherited porosity and internal cracks from nanoscale hybridization with *n*HAp and Ag_2O using MacKenzie and Salganik equations [95],[96],[97], respectively, resulting in a correct elastic modulus of 1.75 GPa and Poisson's ratio of 0.3. The computational compressive force-displacement response agrees well with the experimental results, as shown in **Fig. 5a** while providing insights into the deformation distribution within the representative gyroid unit cell. The FEA model was then extended to account for the effect of other molecular decoration

levels on the compressive response, affirming the stiffening effect of *n*HAp and the softening byproduct of antibacterial silver nanoparticles. Hence, this FEA modeling approach has been validated and calibrated to explore a range of TPMS geometries compared to bone (from different anatomical locations) properties.

The bone microstructure encompasses a broad range of topologies, depending on gender, age, and prognosis, which has been a research focus for biomechanicians and biophysicists alike. Hence, three additional TPMS structures (Diamond, IW-P, and Fischer-Koch) were computationally investigated, **Fig. 5b-*i***, due to their resemblance to bone microstructure from different anatomical sites [98],[99]. The simulation boundary conditions and materials assignment faithfully followed the settings used to compare the numerical and experimental results based on the abovementioned gyroid structure. The Diamond, IW-P, and Fischer-Koch TPMS lattices exhibited higher compressive stiffnesses (**Fig. 5b-*ii***) than the gyroid counterparts, ranging between 600-1000 N/m. Overall, the compressive stiffnesses of the TPMS structures considered herein are compared to the bone stiffness from the entire tested skull frontally and laterally [100], the whole vertebral body [101], and femoral trabecular [102], being remarkably similar to the latter, as summarized in **Fig. 5b-*ii***. At the outset, the FEA model was further leveraged to explore the sensitivity of the bone microstructure resembled by TPMS structures to Poisson's ratio, given the inherent tunability of *osseoPRINT*, by adjusting the weight percentage of high *Mw* PMMA. The computational simulations were repeated while varying the Poisson's ratio between 0.30, 0.35, and 0.40, *i.e.*, within the range of values known for PMMA. The compressive force-displacement results are summarized in **Fig. 5c**, showing dependence on the TPMS geometry and apparent insensitivity to the Poisson's ratio. The results also evidence the suitability and adaptability of *osseoPRINT* for additive manufacturing of bone surrogates and implants, irrespective of the anatomical complexity, *a leap toward personalized medicine*. Advanced material systems, the additive mindset, and the pursuit of a viable and practical pathway to personalized medicine unlock the possibility of easily tailoring implants, envisioned in **Fig. 5d**, by combining different configurations and geometries to precisely mimic the bone structure and mechanics.

5a **Experimental/computational behavior of gyroids**

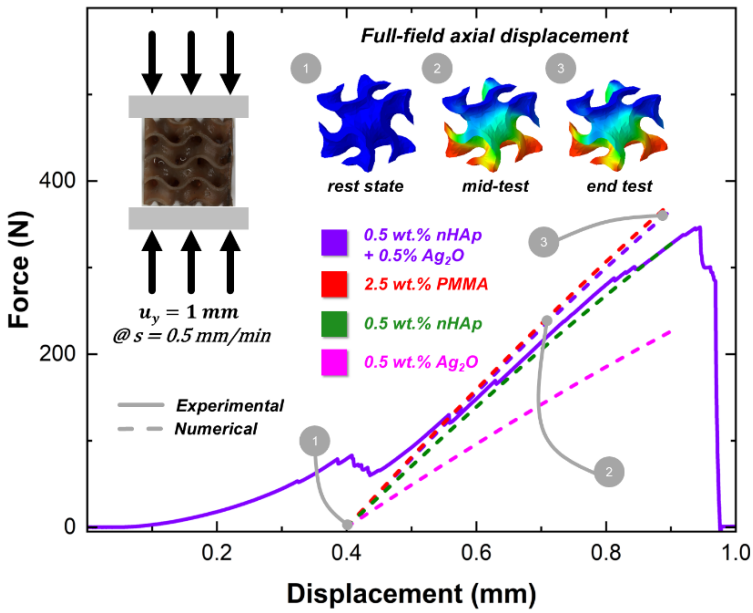

5b **Computational exploration of bone microstructure resembling TPMS geometries**

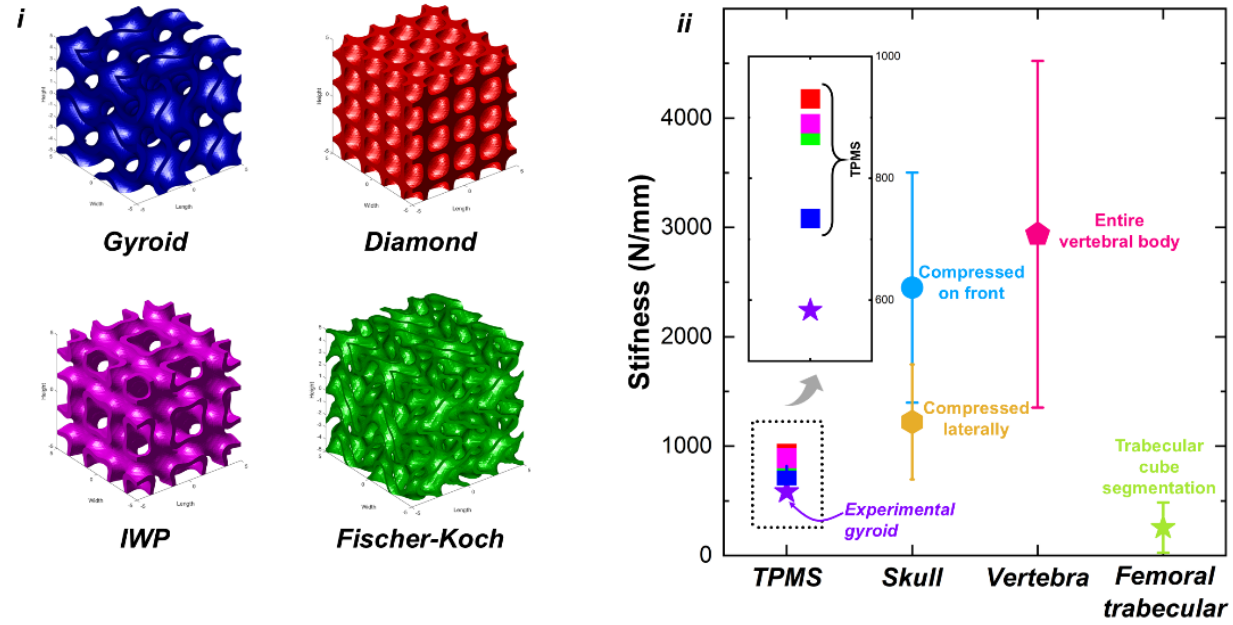

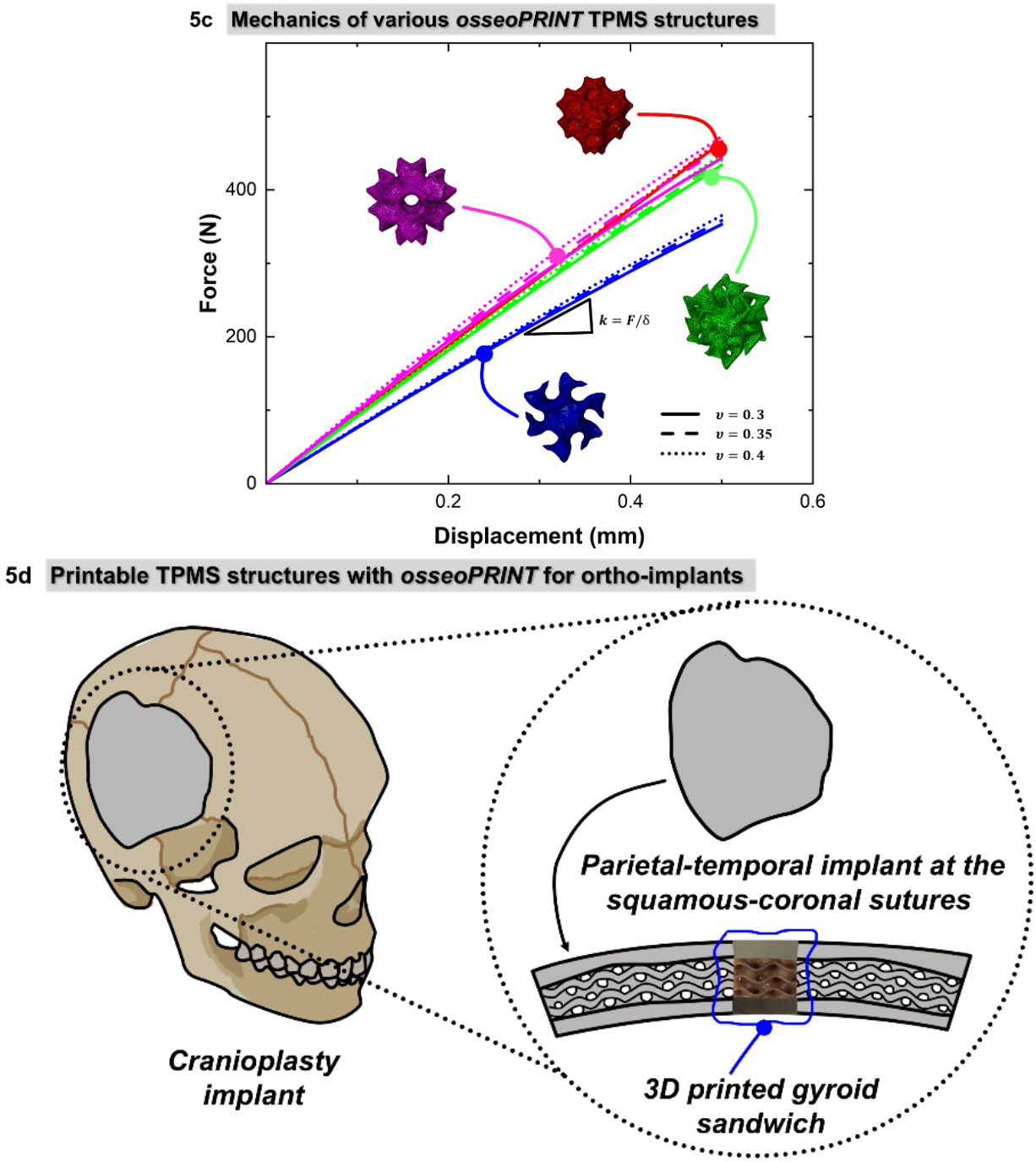

Fig. 5. Patient-specific, anatomically relevant implants using *osseoPRINT* resins with osteoinductive and antibacterial agents to potentially improve bio-acceptability. (a) Comparison between experimental and computational mechanics of 3D printed gyroid structures, representing bone microstructure and elucidating the reliability of the numerical model, which can be tuned as a function of the photocurable resin properties. (b) Computational exploration of several common triply periodic minimum surface topologies based on other variations of bone structures, comparing the compressive stiffnesses (deduced from the numerical results based on *osseoPRINT* properties) with biological tissue properties. (c) Compressive force-displacement of gyroids, Schwarz diamond, IWP, and Fischer-Koch TPMS structures based on the computational results as a function of Poisson's ratio, showing the predictive capabilities of the FEA model. (d) Demonstrative of personalized medicine application, where an envisioned

cranioplasty implant (parietal-temporal implant at the squamous-coronal sutures) can be readily 3D printed using *osseoPRINT*.

3. Conclusion

This study presents a comprehensive approach to designing, synthesizing, and characterizing innovative biocompatible resins tailored for additively manufactured personalized skeletal implants, specifically employing vat photopolymerization techniques. The research thoroughly examined the rheological impact of incorporating PMMA within an MMA-EGDMA crosslinked framework while optimizing the fabrication process under inert atmospheric conditions. All weight percentage formulations demonstrated superior printability and exhibited thermomechanical properties suitable for the intended application as a function of physiological operating conditions. Notably, resins with lower PMMA content exhibited enhanced mechanical stability due to increased crosslinked chain density. Further advancement involved integrating osteoinductive and antibacterial agents to enhance the inherent bioinertness of the new printable photocurable resin, unlocking the transitional potential of this novel photocurable material system. This refinement led to the development of printed structures that closely mimic bone tissue at both macro- and nanoscale levels, which is crucial for effective tissue integration and the prevention of stress shielding. The final formulation, comprising 0.5 *wt.*% *n*HAp and 0.5 *wt.*% Ag_2O within a 2.5 *wt.*% PMMA matrix was utilized to validate the printability and performance of complex structures. The resulting lattices, exhibiting mechanical properties akin to trabecular bone, underscore the adaptability and potential of this personalized bone repair framework, paving the way for the development of easily printable and customizable implants.

4. Experimental section

***Materials*:** All materials were used as received, with no modifications or purifications. MMA (W400201, Sigma-Aldrich), EGDMA (335681, Sigma-Aldrich) and PMMA (445746, Sigma-Aldrich) were used for the synthesis of the base resin. Two extra dopant compounds were added to the base resin *a posteriori*, antibacterial silver nanoparticles, Ag_2O, (221163, Sigma Aldrich), and osseoinducive agent, HAp nanoparticles, (677418, Sigma Aldrich). Phenylbis(2,4,6-trimethylbenzoyl) phosphine oxide (511447, Sigma Aldrich) was the photoinitiator to induce the photocuring process.

***osseoPRINT resin preparation*:** Five generations of printable resins were prepared with different functional modifiers. The base resins, MMA and EGDMA (50:50) with PMMA (0,

2.5, 5, 7.5, and 10 *wt.* %), were mixed in a magnetic stirrer for 3 h and 30 min at 300 rpm and 50 ºC. The photoinitiator was then mixed to enable stereolithography-based printing using a planetary centrifugal mixer (Thinky Mixer, Thinky) at 2000 rpm for 3 min. Resins with the remaining dopant compounds (Ag_2O and HAp) were synthesized faithfully following the previous steps.

***Printing and curing*:** A modified mSLA (*Masked Stereolithography*) 3D printer (Anycubic Photon Mono 2, Anycubic) was used throughout this research. It is imperative to perform the additive manufacturing process under an inert atmosphere to prevent potential chemical attacks to the uncured samples, hence the modification with a closed-circuit nitrogen flow (0.75 MPa and 1.5 l/min). All 3D printing was done using previously optimized parameters, including 30-80 s exposure times for the bottom layers and 10-60 s for the remaining ones, depending on the composition. Printed specimens were cured in an oven for 40 min at 60 ºC under a UV lamp (6 high-power 405nm UV LEDs).

***Characterization*:** The rheological properties of all *osseoPRINT* resin generations were analyzed with a **rheometer** (Discovery HR 30, TA Instruments) with a parallel plate configuration (Ø25 mm) as a function of shear rate (0.1 s^{-1} to 100 s^{-1}). The rheological measurements were done at ambient conditions with a geometrical gap of 0.2 mm. The exact measurements were repeated after extended conditioning in the ambient environment to assess the lifetime of the *osseoPRINT* resins. The thermal properties of the additively manufactured *osseoPRINT* resins were quantified using **differential scanning calorimetry** (DSC 25, TA Instruments) over a temperature history extending from -120 ºC to 400 ºC at a heating rate of 3 ºC/min. A 9.6-10.4 mg of powderized *osseoPRINT* samples were loaded in an aluminum crucible for the DSC measurements. The physicochemical composition of the printed samples was probed with **FTIR spectroscopy** (Nicolet iS5, Thermo Fischer Scientific) over a wavenumber range of 400 cm^{-1} to 4000 cm^{-1}. The viscoelastic properties of 60 × 13 × 1.85 mm plates were characterized in a **dynamic mechanical analyzer** (Discovery DMA 850, TA Instruments) using a dual cantilever beam configuration at 1 Hz and 10 μm amplitude as a function of temperature (35 ºC to 190 ºC) at a heating rate of 5 ºC/min. **Nanoindentation** experiments (NanoTest Vantage, Micro Materials) were carried out to complete the mechanical inspection with a load of 100mN. Finally, miniaturized gyroid structures (emulating internal bone microstructure) were **designed** using MSLattice and mechanically tested under **quasi-static compressive loading** (Instron 5843, Instron) with a crosshead speed of 0.5 mm/min.

Acknowledgments

The authors acknowledge the support of the National Science Foundation under Grant No. 2035663. The authors are also grateful for internal funding from San Diego State University. Funding from the United States Department of Defense (W911NF1410039, W911NF1810477, W911NF2310150, and N00174-23-1-0009) is also acknowledged. Additionally, this work was supported by the MCIN/AEI/10.13039/501100011033 and "European Union NextGenerationEU/PRTR" under grant PDC2021-121368-C21; the MCIN/AEI/10.13039/501100011033 under grants PID2020-112628RA-I00 and PID2020-118480RB-C22; and by the Generalitat Valenciana under grant CIAPOS/2021/271.

Supporting Information
Supporting Information is available from the Wiley Online Library or from the author.

Conflict of Interest
All authors declare no conflict of interest.

Data Availability Statement
The data that support the findings of this study are available from the corresponding author upon reasonable request.

Keywords
personalized medicine, advanced polymer nanocomposites, bio 3D printing, molecular decorations, patient-specific implants

Bibliography
[1] X. Wang, X. Wang, Z. Xiang, Y. Zeng, F. Liu, B. Shao, T. He, J. Ma, S. Yu, L. Liu, *Front. Oncol.* **2021**, *11*, 698773.
[2] J. Wang, Y. Zhang, N. H. Aghda, A. R. Pillai, R. Thakkar, A. Nokhodchi, M. Maniruzzaman, *Advanced Drug Delivery Reviews* **2021**, *174*, 294.
[3] N. C. Paxton, *3D Print Med* **2023**, *9*, 9.
[4] P. Bertsch, M. Diba, D. J. Mooney, S. C. G. Leeuwenburgh, *Chem. Rev.* **2023**, *123*, 834.
[5] Z. Zheng, P. Liu, X. Zhang, Jingguo Xin, Yongjie Wang, X. Zou, X. Mei, S. Zhang, S. Zhang, *Materials Today Bio* **2022**, *16*, 100402.
[6] S. Shih, C. Askinas, S. Caughey, N. Vernice, N. Berri, X. Dong, J. A. Spector, *Journal of Plastic, Reconstructive & Aesthetic Surgery* **2023**, *83*, 266.
[7] R. Guo, M. Morimatsu, T. Feng, F. Lan, D. Chang, F. Wan, Y. Ling, *Stem Cell Res Ther* **2020**, *11*, 19.
[8] B. Chen, Q. Li, B. Zhao, Y. Wang, *Stem Cells Translational Medicine* **2017**, *6*, 1753.
[9] Y. Yu, R.-X. Wu, Y. Yin, F.-M. Chen, *J. Mater. Chem. B* **2016**, *4*, 569.
[10] S. Li, S. Liu, X. Wang, *ijb* **2022**, *8*, 588.
[11] A. A. Al-Tamimi, H. Almeida, P. Bartolo, *Prog Addit Manuf* **2020**, *5*, 95.
[12] M. Arbatti, X. Shan, Z. -Y. Cheng, *Advanced Materials* **2007**, *19*, 1369.
[13] A. J. T. Teo, A. Mishra, I. Park, Y.-J. Kim, W.-T. Park, Y.-J. Yoon, *ACS Biomater. Sci. Eng.* **2016**, *2*, 454.
[14] D. Shekhawat, A. Singh, A. Bhardwaj, A. Patnaik, *IOP Conf. Ser.: Mater. Sci. Eng.* **2021**, *1017*, 012038.
[15] S. Ajmal, F. Athar Hashmi, I. Imran, *Materials Today: Proceedings* **2022**, *62*, 385.
[16] S. K. Powell, R. L. J. Cruz, M. T. Ross, M. A. Woodruff, *Advanced Materials* **2020**, *32*, 2001122.
[17] S. V. Gohil, S. Suhail, J. Rose, T. Vella, L. S. Nair, in *Materials for Bone Disorders*, Elsevier, **2017**, pp. 349–403.

[18] L. Tomazela, M. A. E. Cruz, L. A. Nascimento, C. C. Fagundes, M. A. M. S. Da Veiga, A. Zamarioli, M. Bottini, P. Ciancaglini, M. S. Brassesco, E. E. Engel, A. P. Ramos, *J Biomedical Materials Res* **2022**, *110*, 812.
[19] A. Wazeer, A. Das, A. Sinha, K. Inaba, S. Ziyi, A. Karmakar, *Prog Addit Manuf* **2023**, *8*, 857.
[20] K. K, S. Karuppudaiyan, S. Roy, *Biomed. Phys. Eng. Express* **2023**, *9*, 065020.
[21] E. A. Guzzi, M. W. Tibbitt, *Advanced Materials* **2020**, *32*, 1901994.
[22] V. Schimpf, A. Asmacher, A. Fuchs, B. Bruchmann, R. Mülhaupt, *Macromolecules* **2019**, *52*, 3288.
[23] V. S. D. Voet, T. Strating, G. H. M. Schnelting, P. Dijkstra, M. Tietema, J. Xu, A. J. J. Woortman, K. Loos, J. Jager, R. Folkersma, *ACS Omega* **2018**, *3*, 1403.
[24] R. Setter, S. Schmölzer, N. Rudolph, E. Moukhina, K. Wudy, *Polymer Engineering & Sci* **2023**, *63*, 2180.
[25] V. S. Seesala, L. Sheikh, B. Basu, S. Mukherjee, *ACS Biomater. Sci. Eng.* **2024**, acsbiomaterials.4c00779.
[26] C. Schabowsky, *Polymethyl Methacrylate Safety Profile*, **2021**.
[27] 1.
[28] J. A. Killion, L. M. Geever, D. M. Devine, J. E. Kennedy, C. L. Higginbotham, *Journal of the Mechanical Behavior of Biomedical Materials* **2011**, *4*, 1219.
[29] S.-Y. Chang, T. Ching, M. Hashimoto, *Materials Today: Proceedings* **2022**, *70*, 179.
[30] C. I. Vallo, G. A. Abraham, T. R. Cuadrado, J. San Román, *J Biomed Mater Res* **2004**, *70B*, 407.
[31] K. Mijnendonckx, N. Leys, J. Mahillon, S. Silver, R. Van Houdt, *Biometals* **2013**, *26*, 609.
[32] L. M. Stabryla, K. A. Johnston, N. A. Diemler, V. S. Cooper, J. E. Millstone, S.-J. Haig, L. M. Gilbertson, *Nat. Nanotechnol.* **2021**, *16*, 996.
[33] B. N. Rashmi, S. F. Harlapur, B. Avinash, C. R. Ravikumar, H. P. Nagaswarupa, M. R. Anil Kumar, K. Gurushantha, M. S. Santosh, *Inorganic Chemistry Communications* **2020**, *111*, 107580.
[34] Y. Liu, B. Rath, M. Tingart, J. Eschweiler, *J Biomedical Materials Res* **2020**, *108*, 470.
[35] R. Shanmugam, L. Thangavelu, R. Duraisamy, D. Ganapathy, *World Journal of Dentistry* **2024**, *15*, 79.
[36] I. Ratha, P. Datta, V. K. Balla, S. K. Nandi, B. Kundu, *Ceramics International* **2021**, *47*, 4426.
[37] J. Anita Lett, S. Sagadevan, I. Fatimah, M. E. Hoque, Y. Lokanathan, E. Léonard, S. F. Alshahateet, R. Schirhagl, W. C. Oh, *European Polymer Journal* **2021**, *148*, 110360.
[38] S. M. Oskui, G. Diamante, C. Liao, W. Shi, J. Gan, D. Schlenk, W. H. Grover, *Environ. Sci. Technol. Lett.* **2016**, *3*, 1.
[39] T. G. Fox, H. W. Schnecko, *Polymer* **1962**, *3*, 575.
[40] X. Sun, Y. Y. Chiu, L. J. Lee, *Ind. Eng. Chem. Res.* **1997**, *36*, 1343.
[41] C. T. W. Meereis, F. B. Leal, G. S. Lima, R. V. De Carvalho, E. Piva, F. A. Ogliari, *Dental Materials* **2014**, *30*, 945.
[42] A. Vyas, V. Garg, S. B. Ghosh, S. Bandyopadhyay-Ghosh, *Materials Today: Proceedings* **2022**, *62*, 1435.
[43] Y. Luo, G. Le Fer, D. Dean, M. L. Becker, *Biomacromolecules* **2019**, *20*, 1699.
[44] D. Ahn, L. M. Stevens, K. Zhou, Z. A. Page, *Advanced Materials* **2021**, *33*, 2104906.
[45] B. E. Rapp, in *Microfluidics: Modelling, Mechanics and Mathematics*, Elsevier, **2017**, pp. 243–263.
[46] A. K. Ho, I. Iin, P. A. Gurr, M. F. Mills, G. G. Qiao, *Polymer* **2005**, *46*, 6727.
[47] A. Martini, U. S. Ramasamy, M. Len, *Tribol Lett* **2018**, *66*, 58.
[48] N. Marx, A. Ponjavic, R. I. Taylor, H. A. Spikes, *Tribol Lett* **2017**, *65*, 106.
[49] A. Bagheri Saed, A. H. Behravesh, S. Hasannia, S. A. Alavinasab Ardebili, B. Akhoundi, M. Pourghayoumi, *Journal of Manufacturing Processes* **2020**, *56*, 550.
[50] S. Jiang, X. Liu, Y. Liu, J. Liu, W. He, Y. Dong, *Journal of Photochemistry and Photobiology B: Biology* **2020**, *202*, 111677.

[51] O. A. Osuchukwu, A. Salihi, I. Abdullahi, B. Abdulkareem, C. S. Nwannenna, *SN Appl. Sci.* **2021**, *3*, 822.
[52] F. Struyven, M. Sellier, P. Mandin, *International Journal of Hydrogen Energy* **2023**, *48*, 32607.
[53] R. P. King, *Introduction to Practical Fluid Flow*, Butterworth-Heinemann, Oxford Boston, **2002**.
[54] Y. Nakayama, in *Introduction to Fluid Mechanics*, Elsevier, **2018**, pp. 177–201.
[55] D. Ting, in *Thermofluids*, Elsevier, **2022**, pp. 135–160.
[56] H. Xie, P. Wang, J. Wu, *Artificial Cells, Nanomedicine, and Biotechnology* **2019**, *47*, 260.
[57] C. E. Albers, W. Hofstetter, K. A. Siebenrock, R. Landmann, F. M. Klenke, *Nanotoxicology* **2013**, *7*, 30.
[58] A. Zhakeyev, L. Zhang, J. Xuan, in *3D and 4D Printing of Polymer Nanocomposite Materials*, Elsevier, **2020**, pp. 387–425.
[59] S. G. Prasad, C. Lal, *Biointerface Res Appl Chem* **2022**, *13*, 184.
[60] Ismayil, V. Ravindrachary, R. F. Bhajantri, S. D. Praveena, B. Poojary, D. Dutta, P. K. Pujari, *Polymer Degradation and Stability* **2010**, *95*, 1083.
[61] J. C. M. Suarez, E. B. Mano, E. E. Da Costa Monteiro, M. I. B. Tavares, *J of Applied Polymer Sci* **2002**, *85*, 886.
[62] V. Ţucureanu, A. Matei, A. M. Avram, *Critical Reviews in Analytical Chemistry* **2016**, *46*, 502.
[63] C. P. Ennis, R. I. Kaiser, *Phys. Chem. Chem. Phys.* **2010**, *12*, 14902.
[64] M. Manoj, D. Mangalaraj, N. Ponpandian, C. Viswanathan, *RSC Adv.* **2015**, *5*, 48705.
[65] R. N. Panda, M. F. Hsieh, R. J. Chung, T. S. Chin, *Journal of Physics and Chemistry of Solids* **2003**, *64*, 193.
[66] M. Kumar, S. Arun, P. Upadhyaya, G. Pugazhenthi, *Int J Mech Mater Eng* **2015**, *10*, 7.
[67] K. Wondraczek, J. Adams, J. Fuhrmann, *Macro Chemistry & Physics* **2004**, *205*, 1858.
[68] E. V. Thompson, *J. Polym. Sci. A-2 Polym. Phys.* **1966**, *4*, 199.
[69] J. M. León, V. Bernardo, E. Laguna-Gutiérrez, M. Á. Rodríguez-Pérez, *Polymer International* **2020**, *69*, 72.
[70] J. Biroš, T. Larina, J. Trekoval, J. Pouchlý, *Colloid & Polymer Sci* **1982**, *260*, 27.
[71] M. Piątek-Hnat, K. Bomba, *Materials Today Communications* **2020**, *22*, 100734.
[72] T. Lin, Y. Li, J. Wang, J. You, *Polymers* **2021**, *13*, 4138.
[73] Y. Li, Q. Ma, C. Huang, G. Liu, *ms* **2013**, *19*, 147.
[74] L. Zhang, B. Song, S.-K. Choi, Y. Shi, *International Journal of Mechanical Sciences* **2021**, *197*, 106331.
[75] N. Walter, T. Stich, D. Docheva, V. Alt, M. Rupp, *Injury* **2022**, *53*, S69.
[76] P. Agarwal, H. Lee, P. Smeriglio, F. Grandi, S. Goodman, O. Chaudhuri, N. Bhutani, *Nat Biomed Eng* **2021**, *5*, 1472.
[77] C. Taplan, M. Guerre, J. M. Winne, F. E. Du Prez, *Mater. Horiz.* **2020**, *7*, 104.
[78] R. M. Boumbimba, S. Ahzi, N. Bahlouli, D. Ruch, J. Gracio, *Journal of Engineering Materials and Technology* **2011**, *133*, 030908.
[79] J. D. Menczel, R. B. Prime, Eds., *Thermal Analysis of Polymers: Fundamentals and Applications*, Wiley, **2009**.
[80] F. D. Algahtani, R. Alsafi, H. F. Al-Harthi, N. E. Elsser Elhassan, S. Gdaim, M. T. Elabbasy, M. M. El-Desoky, M. K. Ahmed, *Journal of Materials Research and Technology* **2022**, *20*, 60.
[81] J. Zheng, R. Ozisik, R. W. Siegel, *Polymer* **2005**, *46*, 10873.
[82] K. Olonisakin, M. Fan, Z. Xin-Xiang, L. Ran, W. Lin, W. Zhang, Y. Wenbin, *Composite Interfaces* **2022**, *29*, 1071.
[83] F. Elfakhri, R. Alkahtani, C. Li, J. Khaliq, *Ceramics International* **2022**, *48*, 27280.
[84] J. Y. Rho, P. Zioupos, J. D. Currey, G. M. Pharr, *Journal of Biomechanics* **2002**, *35*, 189.
[85] W. Wu, Y. Zhu, W. Chen, S. Li, B. Yin, J. Wang, X. Zhang, G. Liu, Z. Hu, Y. Zhang, *Orthopaedic Surgery* **2019**, *11*, 270.
[86] M. Baldassarri, E. Bonfante, M. Suzuki, C. Marin, R. Granato, N. Tovar, P. G. Coelho, *J Biomed Mater Res* **2012**, *100B*, 2015.

[87] Ş. Çallıoğlu, P. Acar, *Materials Science and Engineering: C* **2020**, *110*, 110715.
[88] X. Zhai, E. A. Nauman, D. Moryl, R. Lycke, W. W. Chen, *Journal of the Mechanical Behavior of Biomedical Materials* **2020**, *103*, 103597.
[89] F. A. Shah, P. Thomsen, A. Palmquist, *Acta Biomaterialia* **2019**, *84*, 1.
[90] H. Li, S. Zhang, S. Huo, H. Tang, B. Nie, X. Qu, B. Yue, *Journal of Orthopaedic Translation* **2020**, *21*, 66.
[91] J. Zhang, X. Chen, Y. Sun, J. Yang, R. Chen, Y. Xiong, W. Hou, L. Bai, *Materials & Design* **2022**, *218*, 110665.
[92] Y. Lu, Z. Cui, L. Cheng, J. Li, Z. Yang, H. Zhu, C. Wu, *Journal of the Mechanical Behavior of Biomedical Materials* **2020**, *112*, 104080.
[93] B. Charbonnier, M. Manassero, M. Bourguignon, A. Decambron, H. El-Hafci, C. Morin, D. Leon, M. Bensidoum, S. Corsia, H. Petite, D. Marchat, E. Potier, *Acta Biomaterialia* **2020**, *109*, 254.
[94] C. Wang, J. Wu, L. Liu, D. Xu, Y. Liu, S. Li, W. Hou, J. Wang, X. Chen, L. Sheng, H. Lin, D. Yu, *Front. Chem.* **2023**, *11*, 1190630.
[95] J. B. Wachtman Jr, **1969**, p. 158.
[96] J. K. Mackenzie, *Proc. Phys. Soc. B* **1950**, *63*, 2.
[97] R. L. Salganik, *Mechanics of Solids* **1973**, *8*, 135.
[98] A. P. G. Castro, J. Santos, T. Pires, P. R. Fernandes, *Macro Materials & Eng* **2020**, *305*, 2000487.
[99] Y. Lu, Y. Huo, J. Zou, Y. Li, Z. Yang, H. Zhu, C. Wu, *Proc Inst Mech Eng H* **2022**, *236*, 1157.
[100] D. W. Thompson-Bagshaw, R. D. Quarrington, C. F. Jones, *Ann Biomed Eng* **2022**, *50*, 1750.
[101] J. Wegrzyn, J.-P. Roux, M. E. Arlot, S. Boutroy, N. Vilayphiou, O. Guyen, P. D. Delmas, R. Chapurlat, M. L. Bouxsein, *Journal of Bone and Mineral Research* **2010**, *25*, 2324.
[102] L. Zheng, X. Huang, C. Li, P. Li, Z. Lin, S. Huang, *Heliyon* **2022**, *8*, e12101.